Elastic instabilities between two cylinders confined in a channel

Manish Kumar¹ and Arezoo M. Ardekani¹

¹Department of Mechanical Engineering, Purdue University, 585 Purdue Mall, West Lafayette, Indiana 47907 USA

Polymeric flow through porous media is relevant in industrial applications such as enhanced oil recovery, microbial mining, and groundwater remediation. Biological processes such as drug delivery and the transport of cells and particles in the body also depend on the viscoelastic flow through porous matrix. Large elastic stresses induced due to confined geometries can lead to elastic instability for the viscoelastic fluid flow through porous media. We have numerically studied viscoelastic flow through a channel having two closely placed cylinders to investigate pore scale elastic instabilities. We have discovered three distinct flow states in the region between the cylinders. These flow states are closely coupled with the topology of the polymeric stress field. The transition between the flow states can be identified with two critical Weissenberg numbers (Wi_{cr1} and Wi_{cr2}), where the Weissenberg number (Wi) is the ratio of elastic to viscous forces. At Wi < Wi_{cr1}, the flow is stable, symmetric and eddy free. For Wi_{cr1} < Wi < Wi_{cr2}, eddies form in the region between the cylinders. We have measured the area occupied by the eddies for different flow conditions and fluid rheological parameters. At Wi > Wi_{cr2}, the eddy disappears and flow around the cylinders becomes asymmetric. We have quantified the flow asymmetry around the cylinders for different flow rates and fluid rheology. We have also studied the effect of cylinders' diameter and separation on eddies' size ($\mathrm{Wi_{cr1}} < \mathrm{Wi} < \mathrm{Wi_{cr2}}$) and flow asymmetry (Wi > Wi_{cr2}). We have also investigated the effect of fluid rheology and cylinders' diameter and separation on the value of critical Weissenberg numbers.

I. INTRODUCTION

Viscoelastic fluids exhibit a mechanical response between elastic solids and viscous fluids due to the presence of polymeric chains or microscopic elastic filaments [1, 2]. The viscoelastic fluid flow through porous media has important industrial applications in enhanced

oil recovery (EOR) [3], groundwater remediation [4, 5] and biofilm formation [6]. The addition of polymers in displacing fluids enhances crude oil recovery [7–12] through different mechanisms [13–15]. Biofilms mechanically behave like viscoelastic materials [16, 17] and the dynamics of biofilms in porous media has important applications in the fields of water treatment, microbial mining, and bioremediation [18–20]. The flow of complex fluids through porous media is also important in biological processes, like drug delivery [21, 22], the transport of cells during mammalian reproduction [23] and the trapping of particles on ciliary surfaces inside the body [24, 25]. The presence of polymers in fluid creates strong elastic stresses in the confined geometries [26], which leads to strong spatiotemporal fluctuations of the flow (i.e., elastic instability) in porous media above a critical Weissenberg number even at negligible inertia [13, 27–29]. The Weissenberg number is a dimensionless number, which characterizes the relative importance of elastic and viscous forces [30].

The porous matrix is made of large empty spaces (i.e., pore) surrounded by obstacles, and these empty spaces are connected with each other through narrow throats. The study of viscoelastic flow through isolated constriction and cross-slot geometries gives some insight into the pore scale flow dynamics in the throat and the pore-body of porous media, respectively [31]. Similarly, the flow around a confined cylinder sheds light on the flow dynamics close to the solid grains and obstacles present in porous media [31, 32]. Elastic instabilities often lead to the formation of unstable eddies upstream of the constriction to relax the extensional stresses [26, 33–35]. The accumulation of elastic stresses leads to the formation of multiple flow states inside cross-slot geometries [36–41]. The viscoelastic fluid flow around a confined cylinder exhibits different flow behaviors depending on the blockage ratio (B_R), where B_R is the ratio of cylinder diameter to channel width. At a large blockage ratio (i.e., $B_R > 0.5$), viscoelastic instability occurs upstream of the cylinder and unstable eddies form similar to viscoelastic flow through the constriction [42–47]. Whereas at a small blockage ratio, instability occurs downstream of the cylinder, and viscoelastic fluid exhibits flow asymmetry around the cylinder due to the formation of long elastic wake [32, 48–52].

The presence of successive interconnected and closely spaced pores and obstacles in realistic porous media strongly affects the flow dynamics [14, 29, 53–65]. For the flow of polymeric fluids through dense pores, polymeric chains do not have enough time to relax before reaching the next pore due to faster advection than relaxation. The Deborah number (De) is used to represent the ratio of polymeric chains' relaxation to the advection time scale,

and viscoelastic interaction between two pores is expected for $De \geq 1$. To study viscoelastic interaction among the pores and obstacles of porous media, the channels consist of a series of expansions-constrictions [26, 31, 66–68] or the array of cylinders [49, 69–72] are generally used as a 1D model of porous geometry [53]. An experimental study of polymeric flow through the channel consisting of two closely placed cylinders with a small blockage ratio $(B_R = 0.12)$ exhibits a bistable flow state, where the formation of eddies occurs in the region between the cylinders above a critical Weissenberg number [70]. The flow of polymeric fluid through a channel consisting of multiple converging and diverging constraints ($B_R = 0.8$) exhibits bistability, where each pore switches stochastically between eddy dominated to eddy free flow state [35]. The detailed numerical analysis of viscoelastic flow through convergingdiverging channel uncovers that the accumulation of elastic stresses as the polymers advect through successive pores creates streaks of high polymeric stress [26]. These streaks resist the flow crossing the region of high polymeric stress and act as a membrane which induces flow separation. The flow separation inside the pore leads to the formation of eddies in the different parts of the pore, which induces multiple persistent flow states (i.e., multistability) inside the pores [26].

Here, we have numerically studied the elastic instabilities in a channel having a pair of closely placed cylinders and uncovered the mechanism of forming multiple stable flow states. We have calculated the local polymeric stress field and discovered a close coupling between the flow state and the topology of the polymeric stress field. Further, we have calculated the local value of Pakdel-McKinley (M) number [73, 74], which gives the location of the sensitive zone inside the channel, where the elastic instability is likely to occur. We have investigated the effect of fluid rheology, blockage ratio, and the separation between the cylinders on the instabilities. We have also measured the transverse transport of fluid in the region between the cylinders, which helps to explain the enhanced transverse dispersion in porous media [63, 64]. This paper has been written in celebration of Prof. Robert Byron Bird's extraordinary contributions on dynamics of polymeric liquids.

II. PROBLEM SETUP AND GOVERNING EQUATIONS

In this work, we have numerically studied the viscoelastic flow through a channel with a pair of closely placed cylinders and investigated the elastic instabilities in the region between

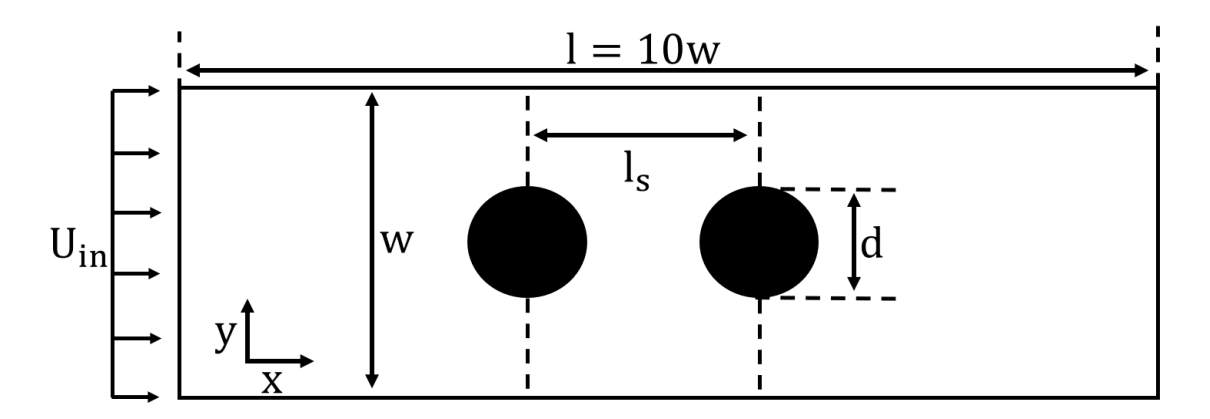


FIG. 1: The schematic of geometry used for numerical simulations. $d = 160\mu m$ is the diameter of the cylinder and $l_s = 2d$ is the center to center distance between cylinders. w = 0.4 mm and l = 4 mm are width and length of the channel, respectively.

two cylinders. The schematic of the geometry used in the simulations has been shown in Fig. 1. The cylinders are located at the center of the channel, and the length of the channel (l) is much larger than the channel's width (w) and cylinders' diameter (d).

The transient flow field of incompressible polymeric solutions through the channel can be described by the conservation of mass and momentum:

$$\nabla \cdot \mathbf{u} = 0, \tag{1}$$

$$\rho \left(\frac{\partial \mathbf{u}}{\partial t} + \mathbf{u} \cdot \nabla \mathbf{u} \right) = -\nabla p + \nabla \cdot \boldsymbol{\tau}, \tag{2}$$

where ρ , \mathbf{u} and p are fluid density, flow field and pressure field, respectively. $\boldsymbol{\tau}$ denotes the total stress tensor, which has the solvent contribution $\boldsymbol{\tau}_s$ and the polymer contribution $\boldsymbol{\tau}_p$, $\boldsymbol{\tau} = \boldsymbol{\tau}_s + \boldsymbol{\tau}_p$. The solvent stress tensor, $\boldsymbol{\tau}_s$, for Newtonian solvents can be calculated as $\boldsymbol{\tau}_s = \eta_s(\nabla \mathbf{u} + \nabla \mathbf{u}^T)$, where η_s is the solvent viscosity. Here, we choose FENE-P constitutive model to describe the extra stresses due to the presence of polymeric chains ($\boldsymbol{\tau}_p$) as FENE-P captures both elasticity and shear-thinning behaviors and includes the finite stretching of the polymeric chains [26, 59, 75–77]. The FENE-P constitutive equation can be given as:

$$\boldsymbol{\tau}_p + \frac{\lambda \nabla}{f} \boldsymbol{\tau}_p = \frac{a\eta_p}{f} (\nabla \mathbf{u} + \nabla \mathbf{u}^T) - \frac{D}{Dt} \left(\frac{1}{f} \right) [\lambda \boldsymbol{\tau}_p + a\eta_p \mathbf{I}], \tag{3}$$

where λ and \mathbf{I} are the relaxation time of the polymer and identity tensor, respectively. $\frac{D}{Dt} = \frac{\partial}{\partial t} + \mathbf{u} \cdot \nabla$ represents the material derivative of the field. η_p is the polymeric contribution to zero-shear rate viscosity, $\eta = \eta_s + \eta_p$, where η is the total viscosity of the solution at zeroshear rate. Function f can be written as:

$$f(\tau_p) = \frac{L^2 + \frac{\lambda}{a\eta_p} tr(\tau_p)}{L^2 - 3},\tag{4}$$

where $a = L^2/(L^2 - 3)$. The extensibility parameter, $L^2 = 3R_0^2/R_e^2$, measures the maximum stretching of the polymer chains, where R_0 and R_e are the maximum allowable length and the equilibrium length of the polymeric chain, respectively [75–78]. The FENE-P model reduces into an Oldroyd-B constitutive model in the limit of $L^2 \to \infty$, which is an excellent model of constant viscosity highly elastic fluids (i.e., Boger fluid[79]) in shear flows [80]. A typical value of the parameter L^2 found in the literature for FENE-P model is in the range of 10-1000 [26, 59, 75, 81, 82]. The hat operator ($^{\nabla}$) used in equation 3 denotes the upper convective time derivative and is given by:

$$\overset{\nabla}{\boldsymbol{\tau}}_{p} = \frac{D\boldsymbol{\tau}_{p}}{Dt} - \boldsymbol{\tau}_{p} \cdot \nabla \mathbf{u} - \nabla \mathbf{u}^{T} \cdot \boldsymbol{\tau}_{p}. \tag{5}$$

The numerical simulations are performed using an open-source framework OpenFOAM [83] integrated with viscoelastic solver RheoTool [84]. The equations are discretized in OpenFOAM [83] using the finite volume method. The log-conformation method has been used to calculate the polymeric stress tensor with higher accuracy and robustness, where the equations are solved for the logarithm of conformation tensor (Θ) instead of τ_p [84, 85]. The log-conformation approach ensures the positive definiteness of the conformation tensor, which is essential for the numerical stability at high Weissenberg numbers [86, 87]. The polymeric stress tensor (τ_p) can be calculated using the log-conformation tensor (Θ) as:

$$\tau_p = \frac{\eta_p}{\lambda} (f e^{\Theta} - a \mathbf{I}). \tag{6}$$

The details of the numerical implementations and the code validations are given in the previous studies [84, 88]. This tool has been successfully used to study viscoelastic instabilities in different geometries [26, 59, 89]. Here, we perform two-dimensional numerical simulations assuming an incompressible and isotropic polymeric fluid. A uniform profile of velocity, null value of polymeric stress tensor (τ_p) and zero-gradient of pressure have been imposed as boundary conditions at the inlet of the channel. For the boundary conditions at the walls and the surface of cylinders, we use no-slip and no-penetration boundary condition for velocity, linear-extrapolation for polymeric stresses and zero normal gradient for pressure [84]. At the outlet, a zero-gradient boundary condition has been used for velocity and

polymeric stress, whereas a constant value has been prescribed for pressure (p = 0). The effect of inlet and outlet boundary conditions on the cylinders is not expected as cylinders are at the center of a long channel.

The Reynolds number (Re) and Weissenberg number (Wi) are relevant dimensionless numbers in this study. The Reynolds number represents the relative importance of inertial and viscous forces, and can be given as $Re = \rho U_{in} d/\eta$, where U_{in} is the inlet velocity. The effect of inertia is negligible in this study as Re < 0.006 (Table I). The Weissenberg number represents the ratio of elastic to viscous forces and following the literature related to the study of cylinder, we define it as Wi = $\lambda U_{in}/d$ [32, 48, 70]. The range of Wi considered in this study is Wi = 0-5 (Table I). The elasticity number (El) represents the ratio of elastic to inertial forces and can be given as $El = Wi/Re = \lambda \eta/\rho d^2$. El is independent of the flow condition and only depends on the fluid properties and geometry length scale. In the present study, elastic forces dominate over the inertial forces as $El \approx 780 >> 1$ (Table I). The Deborah number (De = $\lambda U_{in}/l_s$) can be defined to represent the ratio of relaxation to the advection time scale of polymeric chains in between the cylinders, and its value lies in the range of De = 0.3 - 3 (Table I) in this study. We define $\beta = \eta_s/(\eta_s + \eta_p)$ to characterize the strength of shear thinning of the fluid. We have used λ as the characteristic time scale and U_{in} as the characteristic velocity scale to normalize time (t) and velocity (u) throughout the study. We have normalized the polymeric stress and pressure with the viscous stress scale $(\eta U_{in}/d)$. We have used the pressure drop across the channel as a simple metric to estimate the start-up transient time of the simulation [26] (see Appendix). Fully developed elastic instability occurs for dimensionless time t > 5 (Appendix). We have performed simulations for the maximum dimensionless time $t_{max}=20$ and time interval t=10-20 to calculate the statistics. t_{max} used in the simulations is sufficient for the convergence of the statistics.

ρ	λ	η_s	η_p	U_{in}	L^2
$1000~\rm kg/m^3$	1 s	1 mPa.s	4 - 39 mPa.s	0.1 - 0.75 mm/s	100-1000

TABLE I: The value of different parameters used in the present study.

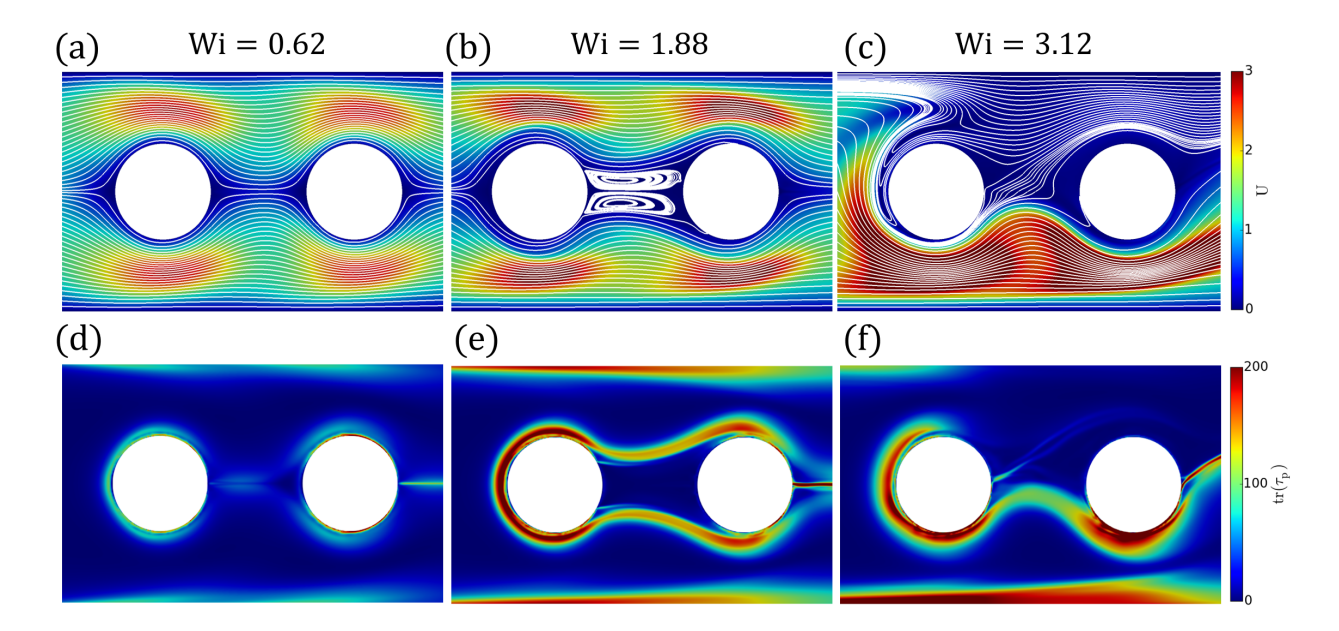


FIG. 2: Streamlines and the magnitude of the velocity field at (a) Wi = 0.62, (b) Wi = 1.88 (Multimedia view) and (c) Wi = 3.12 for the viscoelastic fluid flow through a channel having two cylinders. (d-f) The trace of polymeric stress tensor for the flow states shown in the top panel. Other parameters are $\beta = 0.05$, $L^2 = 1000$ and t = 17.5. The flow achieves steady state for Wi = 0.62.

III. RESULTS AND DISCUSSION

We have studied different flow states induced by elastic instabilities for viscoelastic fluid flow in a channel containing two cylinders aligned with the incident flow direction (Fig. 2). The viscoelastic fluid flow exhibits three distinct states between two cylinders, which can be distinguished by two critical Weissenberg numbers (Wi_{cr1} and Wi_{cr2}). At Wi < Wi_{cr1}, the flow is stable, symmetric and eddy free due to negligible inertia and inadequate elastic stress (flow state type-1) (Fig. 2a). For Wi_{cr1} < Wi < Wi_{cr2}, the eddies appear between two cylinders (type-2) (Fig. 2b (Multimedia view)). This flow state has also been reported in a previous experimental study [70]. At Wi > Wi_{cr2}, the eddy between the cylinders disappears however the flow becomes asymmetric (type-3) (Fig. 2c). The flow states between the cylinders are closely coupled with the polymeric stress field [26]. The trace of polymeric stress tensor (tr(τ_p)) physically represents the stretching of the polymeric chains. The streak of high tr(τ_p) resists the flow crossing the high stress region and leads to flow separation [26]. The flow of polymeric fluid around the cylinder creates an elastic wake behind the cylinder

[32, 48]. At Wi > Wi_{cr1} for the channel of closely placed cylinders, the elastic wake produced by the front cylinder interacts with the second cylinder (Fig. 2). For Wi_{cr1} < Wi < Wi_{cr2}, the elastic wake behind the front cylinder bifurcates and creates two symmetric branches, which extend up to the rear cylinder and encircle the space between the cylinders (Fig. 2e). The region encircled by the streaks of $tr(\tau_p)$ is disconnected from the primary flow, which leads to the flow separation and the formation of eddies in between the cylinders (Fig. 2b). At Wi < Wi_{cr1}, the streak of high $tr(\tau_p)$ does not form (Fig. 2d). Therefore, the flow separation and the formation of eddy between the cylinders do not occur (Fig. 2a). At Wi > Wi_{cr2}, the streak of high $tr(\tau_p)$ is asymmetric and it has a single branch connecting the cylinders (Fig. 2f). This leads to asymmetric flow around the cylinders, and the formation of eddy between the cylinders does not occur (Fig. 2c).

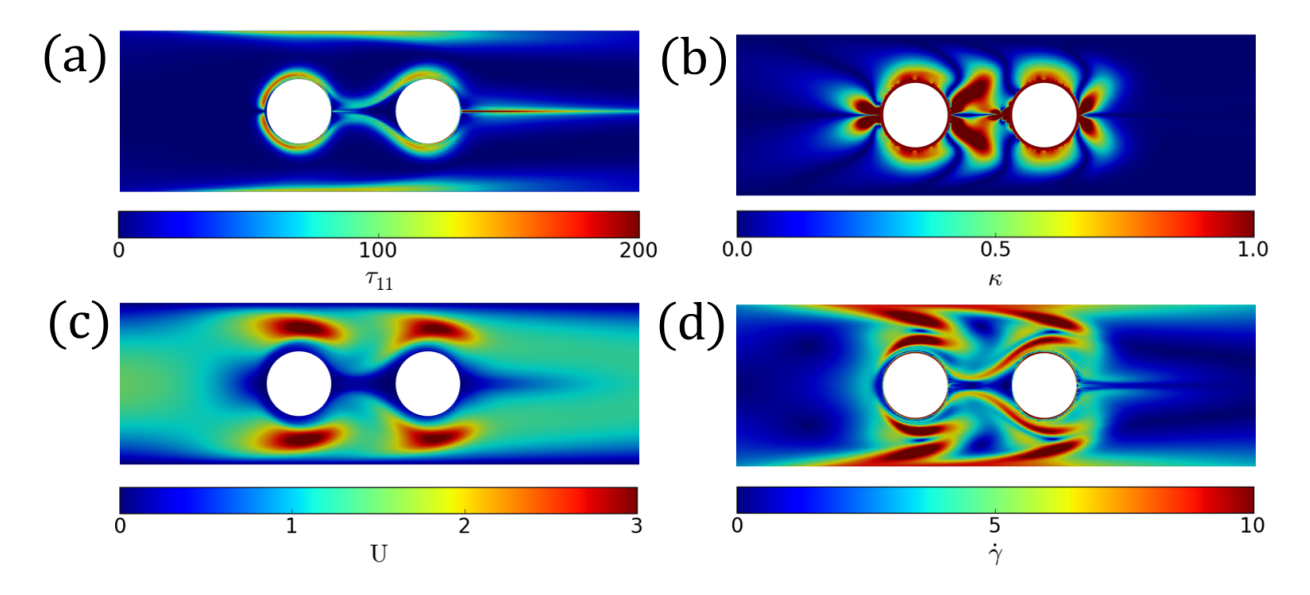


FIG. 3: The contours of (a) tensile stress along the streamline (τ_{11}) , (b) streamline curvature (κ) , (c) velocity field (U) and (d) shear rate $(\dot{\gamma})$ at Wi = 1.25 for $\beta = 0.05$ and $L^2 = 1000$. τ_{11} , κ , U and $\dot{\gamma}$ are normalized with $\eta U_{in}/d$, 2/d, U_{in} and U_{in}/d , respectively. These contours correspond to steady state (t = 17.5).

The Pakdel-McKinley (M) condition [73, 74] is a successfully used criterion to infer the insight of geometry dependent elastic instabilities [29, 41, 48, 90]. The Pakdel-McKinley (M) number is the square root of the product of relevant Weissenberg number and Deborah number, and the criterion of purely elastic instability has been characterized as [73, 74]:

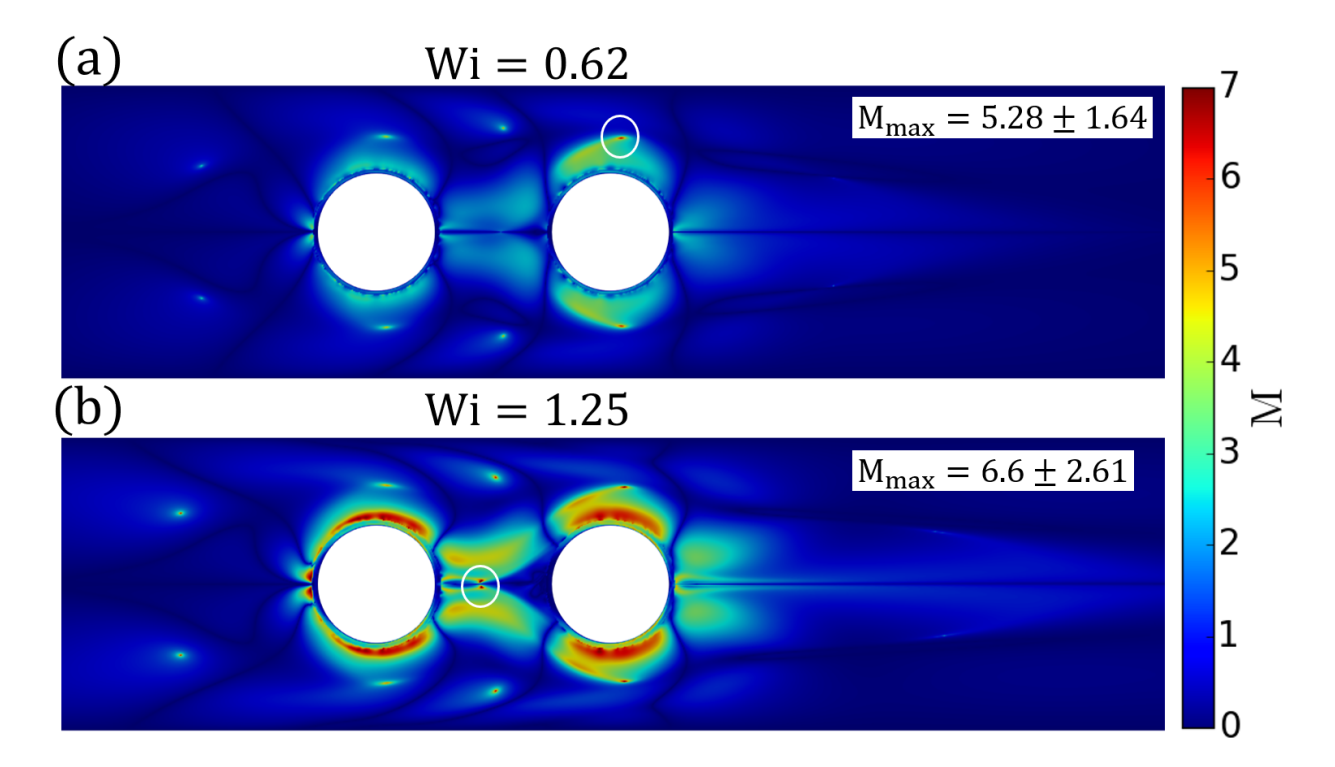


FIG. 4: The contours of Pakdel-McKinley (M) parameter at (a) Wi = 0.62 and (b) Wi = 1.25 for $\beta = 0.05$, L² = 1000 and t = 17.5. White circles indicate the region of maximum value of M (M_{max}). The reported value of M_{max} is the mean and standard deviation obtained over 3×3 ($\approx 2.44 \ \mu m^2$) pixel area centered at the point of maximum value of M [41]. The values of M_{max} are M_{max} = 5.28 ± 1.64 for Wi = 0.62 and M_{max} = 6.6 ± 2.61 for Wi = 1.25.

$$M = \left[\frac{\tau_{11}}{\eta \dot{\gamma}} \lambda U \kappa\right]^{1/2} \geqslant M_{crit},\tag{7}$$

where τ_{11} and $\dot{\gamma}$ are the local tensile stress along the streamline direction and the magnitude of the shear rate, respectively. U is the magnitude of the local velocity field and κ is the local curvature of streamline. τ_{11} can be given as, $\tau_{11} = \mathbf{t} \cdot \boldsymbol{\tau} \cdot \mathbf{t}$, where \mathbf{t} is the unit tangent vector along the streamline. The details of calculation of τ_{11} and κ can be found in previous papers [41, 90]. The contours of different components of M parameter have been shown in Fig. 3. There are multiple streaks of small values of curvature and points of small values of shear rate. We plot the contours of M parameter at Wi < Wi_{cr1} in Fig. 4. The streaks of small values of M correspond to the small value of nominator (τ_{11} , κ , U), whereas the regions of high M value coincide with the small value of denominator ($\dot{\gamma}$). The maximum value

of M (M_{max}) occurs in the top region of the rear cylinder at Wi = 0.62 < Wi_{cr1} (Fig. 4a). However, the location of M_{max} at Wi = 1.25 < Wi_{cr1} has shifted to the region in between the cylinders (Fig. 4b). This indicates that the region in between the cylinders is critical and sensitive to elastic instability at Wi = Wi_{cr1}. Therefore, the formation of new flow state (type-2) at Wi_{cr1} < Wi < Wi_{cr2} occurs due to elastic instability in the region between the cylinders. We plot M_{max} at different Wi (< Wi_{cr1}) in Fig. 5. The reported value of M_{max} is the mean value of M over a square of 3×3 ($\approx 2.44 \mu m^2$) pixel area centered at the point of the maximum value of M [41]. The location of M_{max} abruptly changes from the side of rear cylinder to the region between the cylinders at Wi_M = 1.02 ± 0.08. The change of the location of M_{max} also causes the non-monotonic trend of M_{max} as Wi increases (Fig. 5).

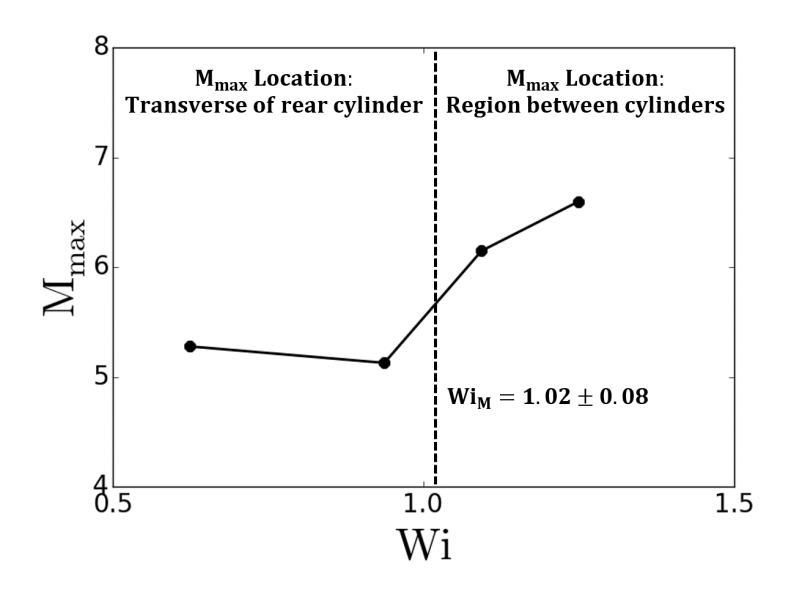


FIG. 5: The value of M_{max} for different Wi (< Wi_{cr1}) at $\beta = 0.05$, $L^2 = 1000$ and t = 17.5.

We have measured the area occupied by the eddies in between the cylinders (i.e., Fig. 2b) for different flow rates and fluid rheological parameters. Fig. 6a depicts the probability density function (PDF) of normalized eddies' area ($A_{\rm eddy}$) for different Wi for a given fluid rheology, where dl_s has been used to normalize $A_{\rm eddy}$. For Wi < Wi_{cr1} or Wi > Wi_{cr2}, the formation of eddy between the cylinders does not occur, therefore $A_{\rm eddy} \approx 0$ (Fig. 6a). The probability distribution of $A_{\rm eddy}$ for Wi_{cr1} < Wi < Wi_{cr2} shows that the mean and the standard deviation of $A_{\rm eddy}$ increase as Wi increases. The power spectral density (PSD) of $A_{\rm eddy}$ is higher for larger Wi (Fig. 6b), which shows that the strength of the temporal fluctuation of $A_{\rm eddy}$ increases with Wi. To quantify the value of critical Wi of the flow state

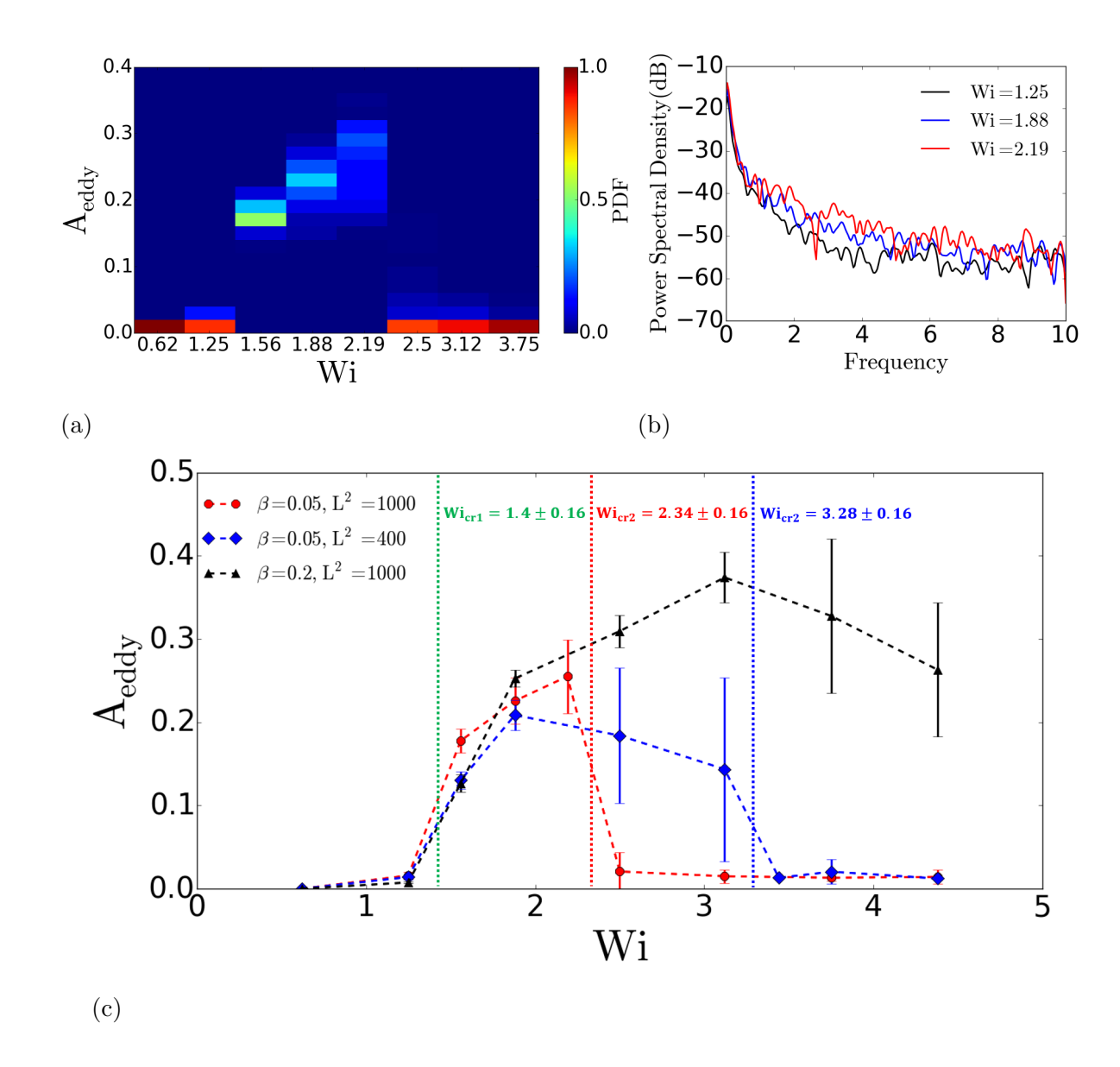


FIG. 6: (a) Probability density function of normalized eddies' area (A_{eddy}) between the cylinders for different Wi for $\beta=0.05$ and $L^2=1000$. (b) Power spectral density of A_{eddy} for $\beta=0.05$ and $L^2=1000$. (c) Mean of normalized eddies' area for different fluid rheological parameters. The standard deviations of A_{eddy} have been shown using error bars at the data points. The area occupied by eddies has been normalized with dl_s .

transition, we have plotted the mean of A_{eddy} in Fig. 6c. The critical Wi of the transition of the flow states can be identified based on the onset of increase/decrease of A_{eddy} . The critical points of the transition of flow states for the fluid of rheological properties $\beta = 0.05$ and $L^2 = 1000$ are $Wi_{cr1} = 1.4 \pm 0.16$ and $Wi_{cr2} = 2.34 \pm 0.16$. We also explore the effect of fluid rheology on the critical Wi. There is no significant effect of fluid rheology on Wi_{cr1} .

However, the value of Wi_{cr2} increases as the value of L decreases or β increases (Fig. 6c). In fact, we do not see the second transition of the flow state (i.e., Wi_{cr2}) at $\beta = 0.2$ and $L^2 = 1000$ for the range of Wi explored in this study. The second transition of the flow state (i.e., Wi_{cr2}) depends on the stability of symmetric branches of elastic wake (Fig. 2e). Strong shear-thinning (low β) destabilizes the elastic wake and hence the eddies between the cylinders. Therefore, Wi_{cr2} decreases as the strength of shear-thinning of fluid increases (i.e., β decreases). The destabilizing effect of shear-thinning has also been seen for a viscoelastic flow around a single confined cylinder [48]. The maximum stretching of polymeric chains increases as L increases, which implies a higher elastic stress at large L. Elastic stress has destabilizing effect on the flow, therefore, Wi_{cr2} decreases as L increases.

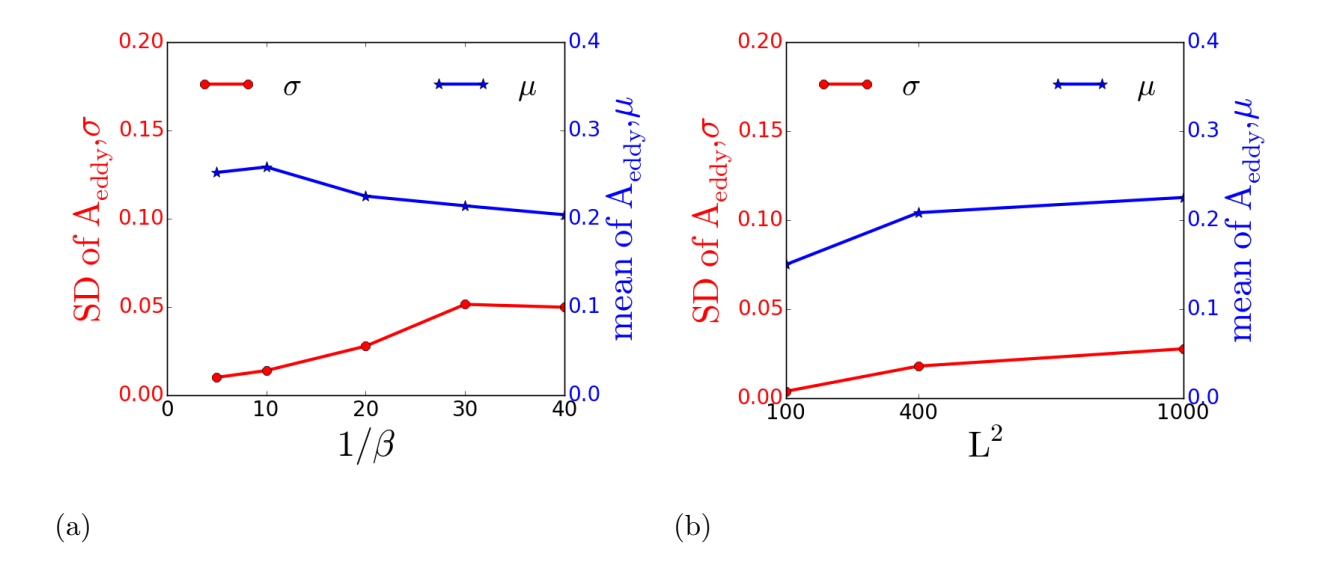


FIG. 7: Mean (μ) and standard deviation (SD, σ) of A_{eddy} at Wi = 1.88 for different values of (a) β and (b) L.

Further, we have explored the effect of β and L on A_{eddy} (Fig. 7a and 7b). As the polymeric contribution in the fluid's zero-shear viscosity (η) increases (i.e., β decreases), the mean of A_{eddy} decreases, whereas the standard deviation of A_{eddy} increases (Fig. 7a). This indicates that the presence of large proportion of polymer destabilizes the eddies in between the cylinders. Therefore, the value of Wi_{cr2} increases as β increases (Fig. 6c). Fig. 7b depicts that both the standard deviation and the mean of A_{eddy} increase as the value of L increases, which also supports the increase of the value of Wi_{cr2} as L decreases (Fig. 6c).

As depicted in Fig. 2c, the flow passing the cylinders becomes asymmetric for Wi > Wi_{cr2}.

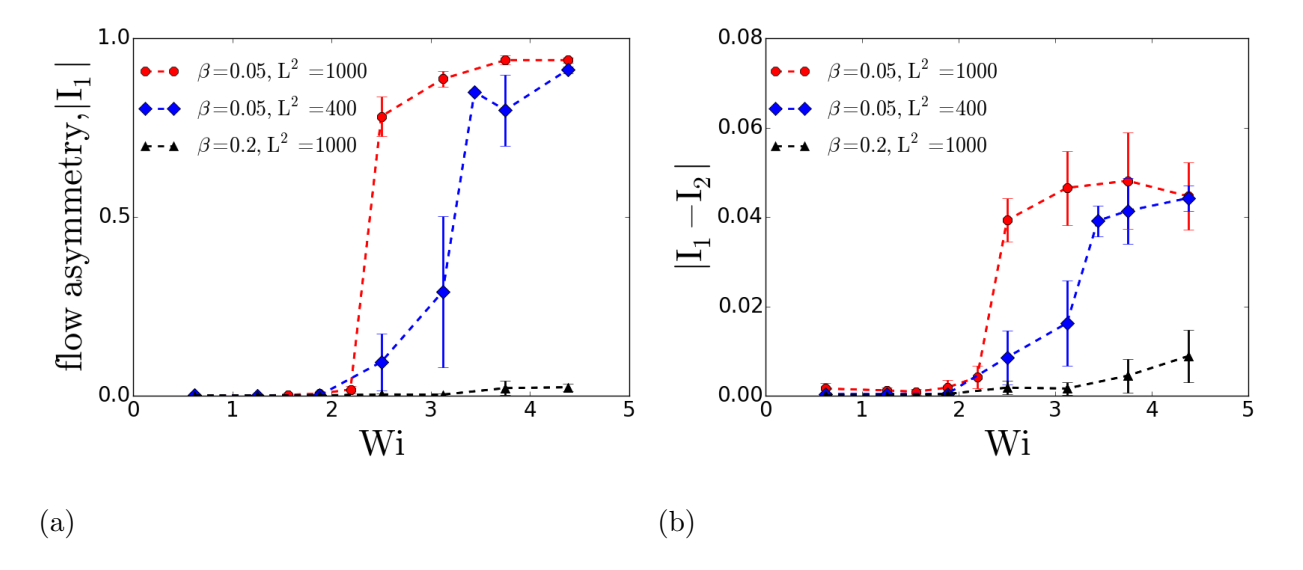


FIG. 8: (a) Flow asymmetry parameter of front cylinder (I_1) for different Wi and fluid rheological parameters. (b) Difference between the asymmetry parameter of front and rear cylinders $(I_1 - I_2)$ for different Wi and fluid rheological parameters.

To quantify this flow asymmetry, we define the asymmetry parameter (I) as:

$$I = (Q_{upper} - Q_{lower})/(Q_{upper} + Q_{lower}), \tag{8}$$

where Q_{upper} (Q_{lower}) is the flow rate through the gap between the cylinder and upper (lower) wall. The value of I varies from I=0 for perfectly symmetric flow to $I=\pm 1$ for the flow passing through either upper or lower gap only. We have calculated the value of the asymmetry parameter (I_1) for the front cylinder for different flow rates and fluid rheological parameters (Fig. 8a). The flow becomes asymmetric for Wi > Wi_{cr2}, and the majority of the fluid passes through either top or bottom gap. For $\beta=0.2$ and $L^2=1000$, the second transition does not happen, therefore asymmetry parameter remains $I_1\approx 0$. In Fig. 2c, we also notice that a small fraction of fluid crosses the region between the cylinders and leads to transverse transport of the fluid. We have plotted the difference between the asymmetry parameter of the front and rear cylinders (I_1-I_2) to quantify the transverse transport of the fluid in the region between the cylinders (Fig. 8b). There is a net transverse transport of fluid in between the cylinders for asymmetric flows, which can explain the increase of transverse dispersion reported in the experiments for polymeric flows through ordered porous media [63, 64]. For $\beta=0.05$ and $L^2=400$, we do not see a sharp increase of I_1 or I_1-I_2 , because there is a range of Wi in which the transition from the flow state of type-2 to

type-3 occurs and in this transition range, both flow states can coexist. We have plotted streamlines at different instances for Wi = 3.12, $\beta = 0.05$ and L² = 400 in Fig. 9. The flow around the cylinders remains symmetric for the formation of eddies between the cylinders (Fig. 9a). However, the formation of smaller eddies in between the cylinders may occur for slightly asymmetric flow around the cylinders (Fig. 9b). Thus, the flow state at Wi = 3.12, $\beta = 0.05$ and L² = 400 (Fig. 9) is transient, where the flow state shown in Fig. 9b is the fusion of type-2 and type-3 flow state. For $\beta = 0.2$ and L² = 1000, the nonzero values of I₁ - I₂ are the result of the formation of amalgam flow state of type-2 and type-3 (Fig. 9b). This is also responsible for a larger standard deviation of A_{eddy} in Fig. 6c for some fluids.

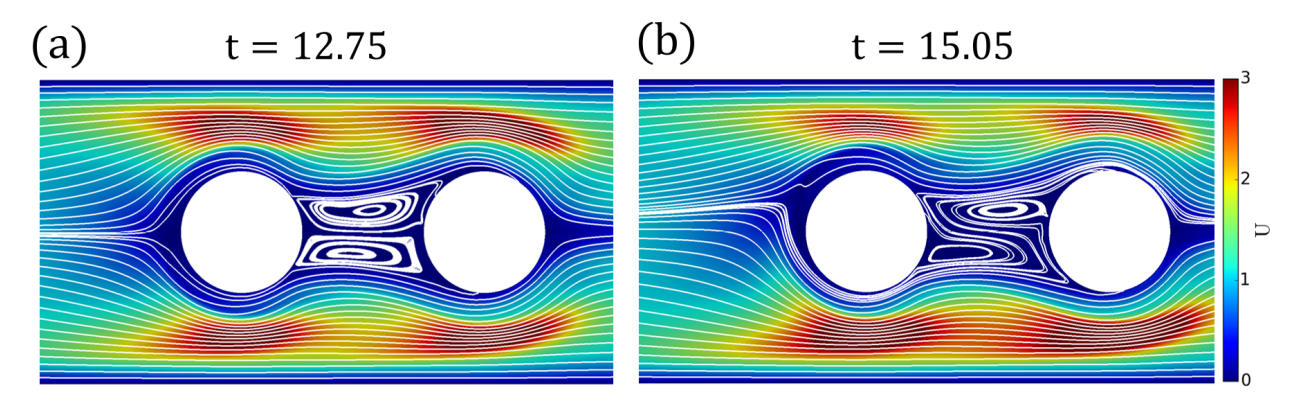


FIG. 9: The streamlines and the magnitude of velocity field at different time instances for Wi = 3.12, $\beta = 0.05$ and L² = 400. (a) Symmetric flow around the cylinders and the eddy formation in between the cylinders (type-2 flow state). (b) Asymmetric flow around the cylinders along with the eddy formation in between the cylinders.

Next, we study the effect of cylinder diameter (d) and the separation between the cylinders (l_s) on the elastic instability. In Fig. 10a, successively we have changed the diameter and the separation between the cylinders and have plotted A_{eddy} for different Wi. First we have changed the diameter of cylinders ($\bar{d} = d/w = 0.2$), while keeping the ratio between the cylinders' separation (l_s) and diameter (d) unchanged ($l_s = 2d$). Wi_{cr1} is not affected by the change in cylinder diameter, whereas the value of Wi_{cr2} has increased from Wi_{cr2} = 2.34 ± 0.16 to Wi_{cr2} = 3.28 ± 0.16 . The value of A_{eddy} also increases as the diameter of cylinders decreases. As the diameter of cylinders decreases the absolute value of l_s also decreases, because $l_s = 2d$. A smaller separation between the cylinders stabilizes the streaks of $tr(\tau_p)$, therefore A_{eddy} and Wi_{cr2} increases as the separation between cylinders decreases (i.e., d decreases) (Fig. 10a). The value of critical Wi required for the flow asymmetry around

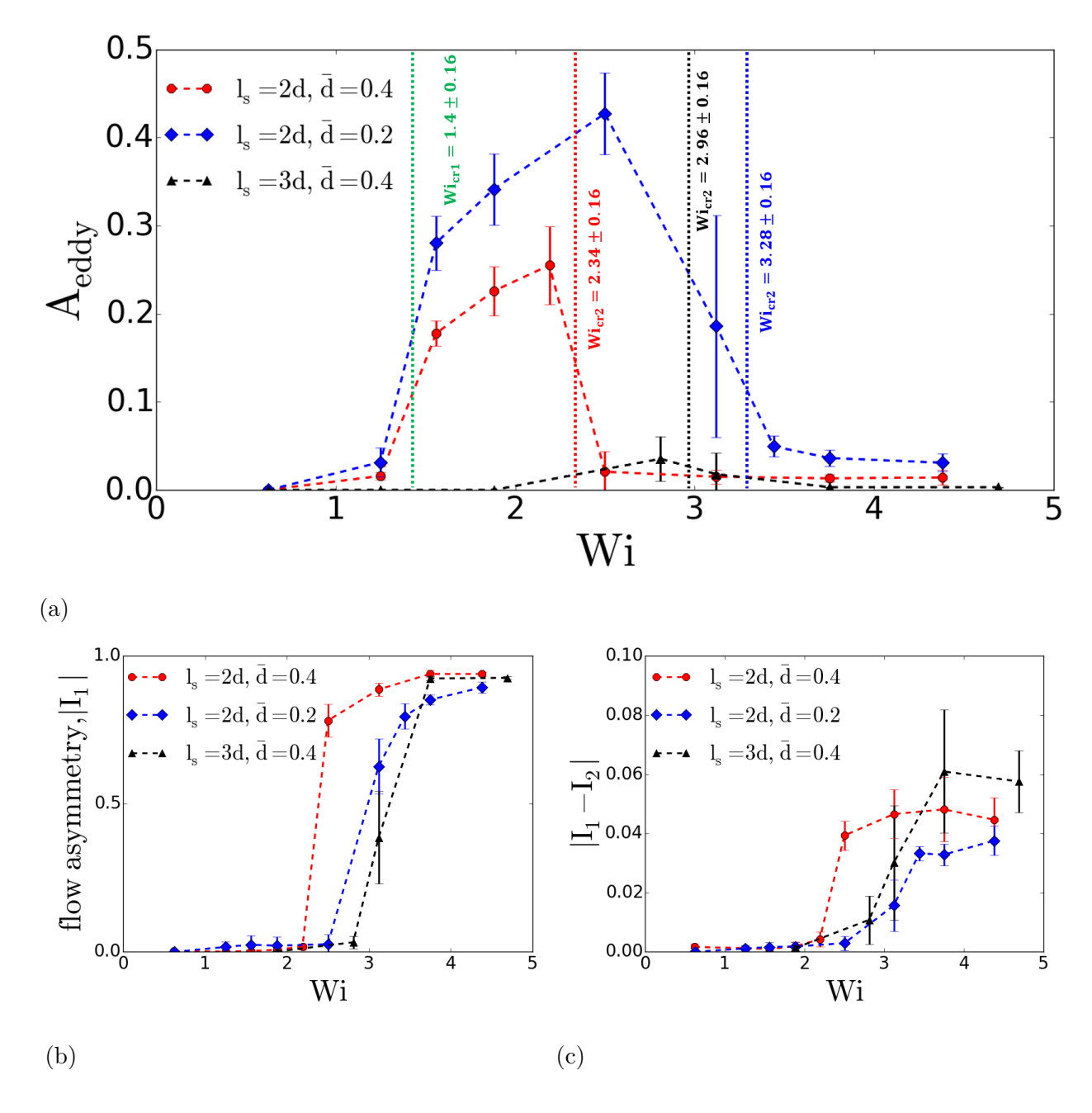


FIG. 10: Mean of (a) A_{eddy} , (b) I_1 and (c) $I_1 - I_2$ for different Wi for varying diameter and separation of cylinders. Other parameters are $\beta = 0.05$ and $L^2 = 1000$. Cylinder diameter in the legend has been normalized with the channel width ($\bar{d} = d/w$).

a single confined cylinder also increases as the cylinder diameter decreases [48]. Next, we change only the separation between the cylinders ($l_s=3d$) and keep cylinders' diameter unchanged ($\bar{d}=0.4$). Here, we notice the transition of flow state directly from type-1 to type-3 and type-2 flow state does not exist. The streaks of $tr(\tau_p)$ become unstable as the

separation between cylinders increases and the formation of stable symmetric branches of $tr(\tau_p)$ in between the cylinders (Fig. 2e) does not occur. Therefore, the eddy formation in between the cylinders does not occur. We have plotted the streamlines and the contours of velocity field for $l_s = 3d$ in Appendix. We have also explored the effect of diameter and separation of cylinders on I_1 (Fig. 10b) and $I_1 - I_2$ (Fig. 10c). The transverse transport $(I_1 - I_2)$ of fluid in between the cylinders increases as the separation between the cylinders increases (Fig. 10c).

IV. CONCLUSIONS

The viscoelastic fluid flow through porous media is essential for enhanced oil recovery and groundwater remediation. We have numerically studied viscoelastic flow through a channel consisting of a pair of closely placed cylinders to shed light on the pore scale elastic instability in porous media. Viscoelastic instabilities induce three distinct flow states in the region between the cylinders, which can be classified by two critical Weissenberg numbers (Wi_{cr1} and Wi_{cr2}), where Weissenberg number (Wi) represents the ratio of elastic to viscous stresses. The formation of streaks of high polymeric stresses induces different flow states in the region between the cylinders. At Wi < Wi_{cr1}, the flow is steady and symmetric due to negligible inertia. For Wi_{cr1} < Wi < Wi_{cr2}, the eddy formation occurs in the region between the cylinders and the area occupied by eddies (A_{eddy}) increases as Wi increases. The mean of A_{eddy} decreases as the shear thinning effect increases (i.e., $\beta = \eta_s/(\eta_s + \eta_p)$ decreases), whereas the standard deviation of A_{eddy} increases with increasing the strength of shear thinning effect. At Wi > Wi_{cr2}, the flow around the cylinders becomes asymmetric, and there is a net transverse transport of fluid in the region between the cylinders. We do not find any significant effect of fluid rheology on Wi_{cr1}, whereas the value of Wi_{cr2} increases as the shear-thinning strength or the extensibility of polymeric chains decreases. The value of Wi_{cr2} also increases as the separation between the cylinders decreases.

V. ACKNOWLEDGMENTS

A.M.A. acknowledges financial support from the National Science Foundation through Grants No. CBET-1700961 and CBET-1705371. Author M.K. acknowledges support from the Ross graduate fellowship from Purdue College of Engineering. This work have used the Extreme Science and Engineering Discovery Environment (XSEDE) [91] for numerical simulations, which is supported by the National Science Foundation Grant No. ACI-1548562 through allocations TG-CTS180066 and TG-CTS190041 to A.M.A.

VI. APPENDIX

A. Start up transient regime

The simulation's start up transient behavior occurs for t < 5 and the instability becomes fully developed for t > 5 as the pressure drop across the channel fluctuates around a well defined mean (Fig. 11).

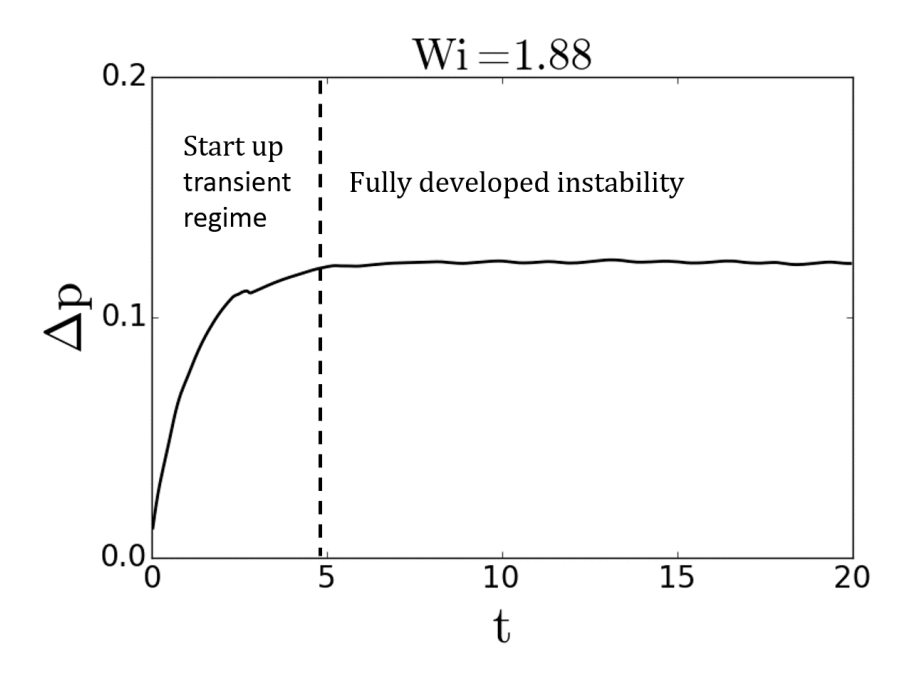


FIG. 11: Dimensionless pressure difference across the channel at Wi = 1.88 for $\beta = 0.05$ and L² = 1000.

B. The streamlines and velocity field at cylinders' separation $l_{\rm s}=3\mathrm{d}$

The stability of eddies decreases as the separation between cylinders increases and hence the viscoelatic flow exhibits only two flow states at $l_s = 3d$ (Fig. 12)

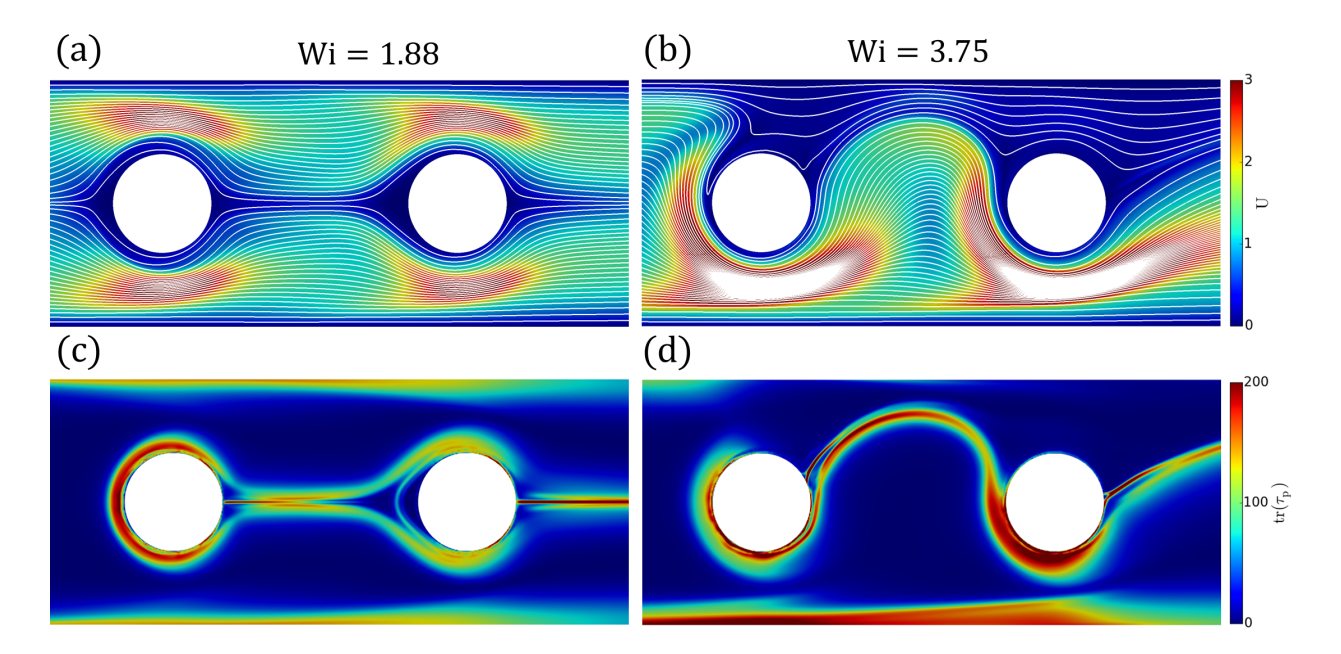


FIG. 12: (a,b) The streamlines and the magnitude of velocity field for different Wi for $l_s = 3d$. (c,d) The trace of polymeric stress tensor for the flow states shown in the top panel. Other parameters are $\beta = 0.05$, $L^2 = 1000$ and t = 17.5.

VII. DATA AVAILABILITY

The data that supports the findings of this study are available within the article and its supplementary material.

 D. T. Chen, Q. Wen, P. A. Janmey, J. C. Crocker, and A. G. Yodh, Rheology of soft materials, Annual review of condensed matter physics 1, 301 (2010).

- [2] L. E. Becker and M. J. Shelley, Instability of elastic filaments in shear flow yields first-normal-stress differences, Physical Review Letters 87, 198301 (2001).
- [3] K. S. Sorbie, *Polymer-improved oil recovery* (Springer Science & Business Media, 2013).
- [4] D. Roote, Technology status report: in situ flushing, Ground Water Remediation Technology Analysis Center (available at http://www.gwrtac.org) (1998).
- [5] M. M. Smith, J. A. Silva, J. Munakata-Marr, and J. E. McCray, Compatibility of polymers and chemical oxidants for enhanced groundwater remediation, Environmental science & technology 42, 9296 (2008).

- [6] M. Carrel, V. L. Morales, M. A. Beltran, N. Derlon, R. Kaufmann, E. Morgenroth, and M. Holzner, Biofilms in 3D porous media: Delineating the influence of the pore network geometry, flow and mass transfer on biofilm development, Water Research 134, 280 (2018).
- [7] B. Sandiford *et al.*, Laboratory and field studies of water floods using polymer solutions to increase oil recoveries, Journal of Petroleum Technology **16**, 917 (1964).
- [8] F. Durst, R. Haas, and B. Kaczmar, Flows of dilute hydrolyzed polyacrylamide solutions in porous media under various solvent conditions, Journal of Applied Polymer Science 26, 3125 (1981).
- [9] M. J. Pitts, T. A. Campbell, H. Surkalo, K. Wyatt, et al., Polymer flood of the rapdan pool, saskatchewan, canada, SPE Reservoir Engineering 10, 183 (1995).
- [10] D. Wang, G. Wang, H. Xia, et al., Large scale high visco-elastic fluid flooding in the field achieves high recoveries, in SPE Enhanced Oil Recovery Conference (Society of Petroleum Engineers, 2011).
- [11] B. Wei, L. Romero-Zerón, and D. Rodrigue, Oil displacement mechanisms of viscoelastic polymers in enhanced oil recovery (eor): a review, Journal of Petroleum Exploration and Production Technology 4, 113 (2014).
- [12] E. Vermolen, M. Van Haasterecht, S. Masalmeh, et al., A systematic study of the polymer visco-elastic effect on residual oil saturation by core flooding, in SPE EOR Conference at Oil and Gas West Asia (Society of Petroleum Engineers, 2014).
- [13] A. Clarke, A. M. Howe, J. Mitchell, J. Staniland, L. A. Hawkes, et al., How viscoelastic-polymer flooding enhances displacement efficiency, SPE Journal 21, 675 (2016).
- [14] S. De, P. Krishnan, J. van der Schaaf, J. Kuipers, E. Peters, and J. Padding, Viscoelastic effects on residual oil distribution in flows through pillared microchannels, Journal of colloid and interface science 510, 262 (2018).
- [15] S. Parsa, E. Santanach-Carreras, L. Xiao, and D. A. Weitz, Origin of anomalous polymer-induced fluid displacement in porous media, Physical Review Fluids 5, 022001 (2020).
- [16] I. Klapper, C. J. Rupp, R. Cargo, B. Purvedorj, and P. Stoodley, Viscoelastic fluid description of bacterial biofilm material properties, Biotechnology and Bioengineering 80, 289 (2002).
- [17] S. Fabbri, D. Johnston, A. Rmaile, B. Gottenbos, M. De Jager, M. Aspiras, E. Starke, M. Ward, and P. Stoodley, Streptococcus mutans biofilm transient viscoelastic fluid behaviour during high-velocity microsprays, Journal of the Mechanical Behavior of Biomedical Materials

- **59**, 197 (2016).
- [18] E. J. Bouwer, H. H. Rijnaarts, A. B. Cunningham, and R. Gerlach, Biofilms in porous media (2000).
- [19] R. Sharp, P. Stoodley, M. Adgie, R. Gerlach, and A. Cunningham, Visualization and characterization of dynamic patterns of flow, growth and activity of biofilms growing in porous media, Water Science and Technology **52**, 85 (2005).
- [20] P. Stoodley, I. Dodds, D. De Beer, H. L. Scott, and J. D. Boyle, Flowing biofilms as a transport mechanism for biomass through porous media under laminar and turbulent conditions in a laboratory reactor system, Biofouling 21, 161 (2005).
- [21] R. Tang, C. S. Kim, D. J. Solfiell, S. Rana, R. Mout, E. M. Velázquez-Delgado, A. Chompoosor, Y. Jeong, B. Yan, Z. J. Zhu, C. Kim, J. A. Hardy, and V. M. Rotello, Direct delivery of functional proteins and enzymes to the cytosol using nanoparticle-stabilized nanocapsules, ACS Nano 7, 6667 (2013).
- [22] A. Parodi, S. G. Haddix, N. Taghipour, S. Scaria, F. Taraballi, A. Cevenini, I. K. Yazdi, C. Corbo, R. Palomba, S. Z. Khaled, J. O. Martinez, B. S. Brown, L. Isenhart, and E. Tasciotti, Bromelain surface modification increases the diffusion of silica nanoparticles in the tumor extracellular matrix, ACS Nano 8, 9874 (2014).
- [23] L. J. Fauci and R. Dillon, Biofluidmechanics of Reproduction, Annual Review of Fluid Mechanics 38, 371 (2006).
- [24] D. J. Smith, E. A. Gaffney, and J. R. Blake, Modelling mucociliary clearance, Respiratory Physiology and Neurobiology 163, 178 (2008).
- [25] W. Stannard and C. O'Callaghan, Ciliary function and the role of cilia in clearance, Journal of Aerosol Medicine 19, 110 (2006), pMID: 16551222.
- [26] M. Kumar, S. Aramideh, C. A. Browne, S. S. Datta, and A. M. Ardekani, Numerical investigation of multistability in the unstable flow of a polymer solution through porous media, Physical Review Fluids 6, 033304 (2021).
- [27] J. Mitchell, K. Lyons, A. M. Howe, and A. Clarke, Viscoelastic polymer flows and elastic turbulence in three-dimensional porous structures, Soft Matter 12, 460 (2016).
- [28] A. M. Howe, A. Clarke, and D. Giernalczyk, Flow of concentrated viscoelastic polymer solutions in porous media: effect of mw and concentration on elastic turbulence onset in various geometries, Soft Matter 11, 6419 (2015).

- [29] D. M. Walkama, N. Waisbord, and J. S. Guasto, Disorder suppresses chaos in viscoelastic flows, Physical Review Letters 124, 164501 (2020).
- [30] K. Weissenberg, A continuum theory of rhelogical phenomena (1947).
- [31] C. A. Browne, A. Shih, and S. S. Datta, Pore-scale flow characterization of polymer solutions in microfluidic porous media, Small, 1903944 (2019).
- [32] S. J. Haward, C. C. Hopkins, and A. Q. Shen, Asymmetric flow of polymer solutions around microfluidic cylinders: Interaction between shear-thinning and viscoelasticity, Journal of Non-Newtonian Fluid Mechanics 278, 104250 (2020).
- [33] L. E. Rodd, T. P. Scott, D. V. Boger, J. J. Cooper-White, and G. H. McKinley, The inertioelastic planar entry flow of low-viscosity elastic fluids in micro-fabricated geometries, Journal of Non-Newtonian Fluid Mechanics 129, 1 (2005).
- [34] A. Lanzaro and X.-F. Yuan, Effects of contraction ratio on non-linear dynamics of semidilute, highly polydisperse paam solutions in microfluidics, Journal of Non-Newtonian Fluid Mechanics 166, 1064 (2011).
- [35] C. A. Browne, A. Shih, and S. S. Datta, Bistability in the unstable flow of polymer solutions through pore constriction arrays, Journal of Fluid Mechanics 890, 10.1017/jfm.2020.122 (2020).
- [36] P. E. Arratia, C. C. Thomas, J. Diorio, and J. P. Gollub, Elastic instabilities of polymer solutions in cross-channel flow, Physical Review Letters **96**, 12 (2006).
- [37] R. J. Poole, M. A. Alves, and P. J. Oliveira, Purely elastic flow asymmetries, Physical Review Letters 99, 1 (2007).
- [38] G. N. Rocha, R. J. Poole, M. A. Alves, and P. J. Oliveira, On extensibility effects in the cross-slot flow bifurcation, Journal of Non-Newtonian Fluid Mechanics **156**, 58 (2009).
- [39] S. J. Haward and G. H. McKinley, Instabilities in stagnation point flows of polymer solutions, Physics of Fluids **25**, 10.1063/1.4818151 (2013).
- [40] S. J. Haward, Microfluidic extensional rheometry using stagnation point flow, Biomicrofluidics 10, 043401 (2016).
- [41] S. J. Haward, G. H. Mckinley, and A. Q. Shen, Elastic instabilities in planar elongational flow of monodisperse polymer solutions, Scientific Reports 6, 1 (2016).
- [42] B. Qin, P. F. Salipante, S. D. Hudson, and P. E. Arratia, Upstream vortex and elastic wave in the viscoelastic flow around a confined cylinder, Journal of Fluid Mechanics 864 (2019).

- [43] Y. Zhao, A. Q. Shen, and S. J. Haward, Flow of wormlike micellar solutions around confined microfluidic cylinders, Soft Matter 12, 8666 (2016).
- [44] F. J. Galindo-Rosales, L. Campo-Deaño, P. C. Sousa, V. M. Ribeiro, M. S. Oliveira, M. A. Alves, and F. T. Pinho, Viscoelastic instabilities in micro-scale flows, Experimental Thermal and Fluid Science 59, 128 (2014).
- [45] S. Kenney, K. Poper, G. Chapagain, and G. F. Christopher, Large deborah number flows around confined microfluidic cylinders, Rheologica Acta **52**, 485 (2013).
- [46] V. Ribeiro, P. Coelho, F. Pinho, and M. Alves, Viscoelastic fluid flow past a confined cylinder: Three-dimensional effects and stability, Chemical engineering science **111**, 364 (2014).
- [47] X. Shi, S. Kenney, G. Chapagain, and G. F. Christopher, Mechanisms of onset for moderate mach number instabilities of viscoelastic flows around confined cylinders, Rheologica Acta 54, 805 (2015).
- [48] S. Varchanis, C. C. Hopkins, A. Q. Shen, J. Tsamopoulos, and S. J. Haward, Asymmetric flows of complex fluids past confined cylinders: A comprehensive numerical study with experimental validation, Physics of Fluids 32, 053103 (2020).
- [49] S. J. Haward, K. Toda-Peters, and A. Q. Shen, Steady viscoelastic flow around high-aspectratio, low-blockage-ratio microfluidic cylinders, Journal of Non-Newtonian Fluid Mechanics 254, 23 (2018).
- [50] S. J. Haward, N. Kitajima, K. Toda-Peters, T. Takahashi, and A. Q. Shen, Flow of wormlike micellar solutions around microfluidic cylinders with high aspect ratio and low blockage ratio, Soft Matter 15, 1927 (2019).
- [51] M. B. Khan and C. Sasmal, Elastic instabilities and bifurcations in flows of wormlike micellar solutions past single and two vertically aligned microcylinders: Effect of blockage and gap ratios, Physics of Fluids **33**, 033109 (2021).
- [52] C. C. Hopkins, S. J. Haward, and A. Q. Shen, Tristability in Viscoelastic Flow Past Side-by-Side Microcylinders, Physical Review Letters **126**, 054501 (2021).
- [53] M. J. Blunt, Multiphase flow in permeable media: A pore-scale perspective (Cambridge University Press, 2017).
- [54] S. S. Datta, H. Chiang, T. Ramakrishnan, and D. A. Weitz, Spatial fluctuations of fluid velocities in flow through a three-dimensional porous medium, Physical review letters 111, 064501 (2013).

- [55] P. K. Kang, P. de Anna, J. P. Nunes, B. Bijeljic, M. J. Blunt, and R. Juanes, Pore-scale intermittent velocity structure underpinning anomalous transport through 3-d porous media, Geophysical Research Letters 41, 6184 (2014).
- [56] T. Pak, I. B. Butler, S. Geiger, M. I. van Dijke, and K. S. Sorbie, Droplet fragmentation: 3d imaging of a previously unidentified pore-scale process during multiphase flow in porous media, Proceedings of the National Academy of Sciences 112, 1947 (2015).
- [57] F. Zami-Pierre, R. De Loubens, M. Quintard, and Y. Davit, Transition in the flow of power-law fluids through isotropic porous media, Physical review letters **117**, 074502 (2016).
- [58] S. Aramideh, P. P. Vlachos, and A. M. Ardekani, Pore-scale statistics of flow and transport through porous media, Physical Review E 98, 1 (2018).
- [59] S. Aramideh, P. P. Vlachos, and A. M. Ardekani, Nanoparticle dispersion in porous media in viscoelastic polymer solutions, Journal of Non-Newtonian Fluid Mechanics 268, 75 (2019).
- [60] S. De, S. Koesen, R. Maitri, M. Golombok, J. Padding, and J. van Santvoort, Flow of viscoelastic surfactants through porous media, AIChE Journal 64, 773 (2018).
- [61] S. De, J. Kuipers, E. Peters, and J. Padding, Viscoelastic flow simulations in random porous media, Journal of Non-Newtonian Fluid Mechanics 248, 50 (2017).
- [62] S. De, J. Kuipers, E. Peters, and J. Padding, Viscoelastic flow simulations in model porous media, Physical Review Fluids 2, 053303 (2017).
- [63] C. Scholz, F. Wirner, J. R. Gomez-Solano, and C. Bechinger, Enhanced dispersion by elastic turbulence in porous media, Epl 107, 10.1209/0295-5075/107/54003 (2014).
- [64] J. D. Jacob, R. Krishnamoorti, and J. C. Conrad, Particle dispersion in porous media: Differentiating effects of geometry and fluid rheology, Physical Review E 96, 1 (2017).
- [65] S. J. Haward, C. C. Hopkins, and A. Q. Shen, Stagnation points control chaotic fluctuations in viscoelastic porous media flow (2021), arXiv:2105.11063 [physics.flu-dyn].
- [66] R. Haas and F. Durst, Viscoelastic flow of dilute polymer solutions in regularly packed beds, Rheologica Acta 21, 566 (1982).
- [67] N. E. Dyakonova, J. A. Odell, Y. V. Brestkin, A. V. Lyulin, and A. E. Saez, Macromolecular strain in periodic models of porous media flows, Journal of Non-Newtonian Fluid Mechanics 67, 285 (1996).
- [68] M. G. Saphiannikova, A. A. Darinskii, and N. E. Dyakonova, Computer simulation of dilute polymer solutions in transient elongational flows, Macromolecular Theory and Simulations 9,

- 270 (2000).
- [69] X. Shi and G. F. Christopher, Growth of viscoelastic instabilities around linear cylinder arrays, Physics of Fluids 28, 124102 (2016).
- [70] A. Varshney and V. Steinberg, Elastic wake instabilities in a creeping flow between two obstacles, Physical Review Fluids 2, 051301 (2017).
- [71] B. Qin and P. E. Arratia, Characterizing elastic turbulence in channel flows at low reynolds number, Physical Review Fluids 2, 083302 (2017).
- [72] C. C. Hopkins, S. J. Haward, and A. Q. Shen, Purely Elastic Fluid-Structure Interactions in Microfluidics: Implications for Mucociliary Flows, Small 16, 1903872 (2020).
- [73] G. H. McKinley, P. Pakdel, and A. Öztekin, Rheological and geometric scaling of purely elastic flow instabilities, Journal of Non-Newtonian Fluid Mechanics 67, 19 (1996).
- [74] P. Pakdel and G. H. McKinley, Elastic instability and curved streamlines, Physical Review Letters 77, 2459 (1996).
- [75] R. B. Bird, P. J. Dotson, and N. L. Johnson, Polymer solution rheology based on a finitely extensible bead-spring chain model, Journal of Non-Newtonian Fluid Mechanics 7, 213 (1980).
- [76] R. Bird, R. Armstrong, and O. Hassager, *Dynamics of polymeric liquids. Vol. 1, 2nd Ed. :*Fluid mechanics (John Wiley and Sons Inc., New York, NY, United States, 1987).
- [77] R. B. Bird, C. F. Curtiss, R. C. Armstrong, and O. Hassager, Dynamics of Polymeric Liquids, Volume 2: Kinetic Theory, 2nd Edition, 2nd ed. (Wiley, 1987).
- [78] B. Purnode and M. J. Crochet, Polymer solution characterization with the FENE-P model, Journal of Non-Newtonian Fluid Mechanics 77, 1 (1998).
- [79] D. Boger, A highly elastic constant-viscosity fluid, Journal of Non-Newtonian Fluid Mechanics 3, 87 (1977).
- [80] J. G. Oldroyd, On the formulation of rheological equations of state, Proceedings of the Royal Society of London. Series A, Mathematical and physical sciences **200**, 523 (1950).
- [81] M. D. Chilcott and J. M. Rallison, Creeping flow of dilute polymer solutions past cylinders and spheres, Journal of Non-Newtonian Fluid Mechanics 29, 381 (1988).
- [82] P. J. Oliveira, An exact solution for tube and slit flow of a FENE-P fluid, Acta Mechanica 158, 157 (2002).
- [83] H. Jasak, A. Jemcov, and Z. Tukovic, Openfoam: A c++ library for complex physics simulations, International Workshop on Coupled Methods in Numerical Dynamics, 1 (2007), cited

- By :275.
- [84] F. Pimenta and M. A. Alves, Stabilization of an open-source finite-volume solver for viscoelastic fluid flows, Journal of Non-Newtonian Fluid Mechanics 239, 85 (2017).
- [85] F. Habla, M. W. Tan, J. Haßlberger, and O. Hinrichsen, Numerical simulation of the viscoelastic flow in a three-dimensional lid-driven cavity using the log-conformation reformulation in OpenFOAM®, Journal of Non-Newtonian Fluid Mechanics 212, 47 (2014).
- [86] R. Fattal and R. Kupferman, Constitutive laws for the matrix-logarithm of the conformation tensor, Journal of Non-Newtonian Fluid Mechanics **123**, 281 (2004).
- [87] R. Fattal and R. Kupferman, Time-dependent simulation of viscoelastic flows at high Weissenberg number using the log-conformation representation, Journal of Non-Newtonian Fluid Mechanics 126, 23 (2005).
- [88] J. L. Favero, A. R. Secchi, N. S. Cardozo, and H. Jasak, Viscoelastic flow analysis using the software OpenFOAM and differential constitutive equations, Journal of Non-Newtonian Fluid Mechanics 165, 1625 (2010).
- [89] M. Davoodi, A. F. Domingues, and R. J. Poole, Control of a purely elastic symmetry-breaking flow instability in cross-slot geometries, Journal of Fluid Mechanics 881, 1123 (2019).
- [90] A. Öztekin, B. Alakus, and G. H. McKinley, Stability of planar stagnation flow of a highly viscoelastic fluid, Journal of Non-Newtonian Fluid Mechanics **72**, 1 (1997).
- [91] J. Towns, T. Cockerill, M. Dahan, I. Foster, K. Gaither, A. Grimshaw, V. Hazlewood, S. Lathrop, D. Lifka, G. Peterson, R. Roskies, J. Scott, and N. Wilkins-Diehr, Xsede: accelerating scientific discovery, Comput. Sci. Eng. 16, 62 (2014).